

# DGIQA: Depth-guided Feature Attention and Refinement for Generalizable Image Quality Assessment

Vaishnav Ramesh, Junliang Liu, Haining Wang, and Md Jahidul Islam

RoboPI laboratory, Department of ECE, University of Florida

Model and code: <https://github.com/uf-robopi/DGIQA> \*

## Abstract

A long-held challenge in no-reference image quality assessment (NR-IQA) learning from human subjective perception is the lack of objective generalization to unseen natural distortions. To address this, we integrate a novel **Depth-Guided** cross-attention and refinement (Depth-CAR) mechanism, which distills scene depth and spatial features into a structure-aware representation for improved NR-IQA. This brings in the knowledge of object saliency and relative contrast of the scene for more discriminative feature learning. Additionally, we introduce the idea of TCB (Transformer-CNN Bridge) to fuse high-level global contextual dependencies from a transformer backbone with local spatial features captured by a set of hierarchical CNN (convolutional neural network) layers. We implement TCB and Depth-CAR as multimodal attention-based projection functions to select the most informative features, which also improve training time and inference efficiency. Experimental results demonstrate that our proposed **DGIQA** model achieves state-of-the-art (SOTA) performance on both synthetic and authentic benchmark datasets. More importantly, **DGIQA** outperforms SOTA models on cross-dataset evaluations as well as in assessing natural image distortions such as low-light effects, hazy conditions, and lens flares.

## 1. Introduction

Image Quality Assessment (IQA) methods provide a means to evaluate the perceptual and statistical *qualities* of images. Traditional full-reference and reduced-reference IQA metrics require an undistorted, high-quality reference image to measure degradation [50], which is generally unavailable in practice. Therefore, Non-Reference IQA (NR-IQA) methods are essential in computer vision and imaging [28, 49, 51], enabling robust prediction of image quality solely based on its *signal* content and statistics [27, 38, 65].

With the recent advances in neural networks and deep visual learning, NR-IQA methods have achieved increasingly

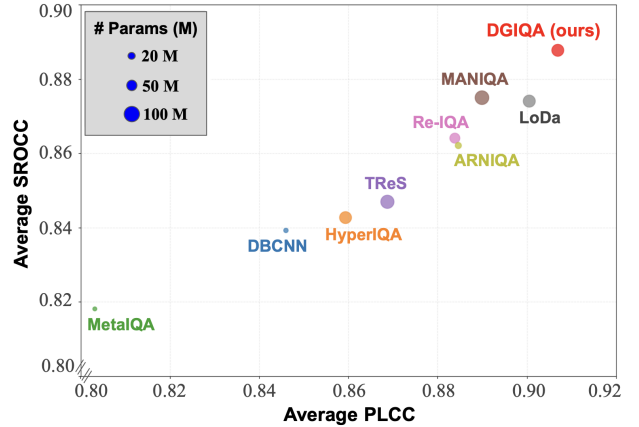


Figure 1. DGIQA demonstrates improved NR-IQA performance over SOTA models for SROCC (Spearman's rank order correlation coefficient) and PLCC (Pearson's linear correlation coefficient) scores averaged over seven benchmark datasets [48, 65]: LIVE, CSIQ, TID2013, Kadid10k, LIVE-C, Koniq10k, and LIVE-FB.

accurate predictions that align closely with subjective human opinion scores, as shown in Fig. 1. But they often fail to generalize to *unseen distortions* or *out-of-distribution* datasets. This limits their effectiveness in real-world scenarios, where distortions often differ significantly from training conditions. This generalization gap may arise because traditional IQA models rely solely on RGB cues and often fail to attend to the perceptually relevant regions in an image, regions that humans naturally prioritize when judging image quality, such as proximal objects and structural boundaries.

In human visual perception, depth plays a critical role in guiding attention toward salient, structurally important content, particularly objects that are closer to the observer. Depth cues have been shown to enhance realism and perceived quality of visual experiences in stereoscopic vision [16]. Beyond perception, depth has been widely used to improve performance in a range of computer vision tasks by providing complementary structural information. In Salient object detection (SOD), additional depth input has shown to boost performance [7, 8, 68]. In semantic segmen-

\*Correspondence: vaishnavramesh@ufl.edu

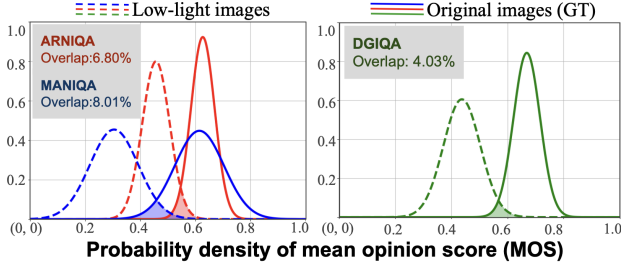


Figure 2. DGIQA performs 41%-50% better separation of IQA score distributions than SOTA models on unseen low-light scenes (LOL dataset [10]); the top transformer model (MANIQA [59]) and CNN model (ARNIQA [1]) are used for baseline comparison.

tation, depth contributes to better boundary localization and scene understanding [21, 73].

In this paper, we introduce Depth-guided Cross-Attention and Refinement (Depth-CAR) mechanism to *filter* and *refine* spatial features based on structural guidance of the scene. It performs a spatial attention-based projection to use depth-guided queries to find object saliency and structural information from RGB features for improved IQA predictions. Additionally, to decrease number of parameters without compromising performance, we design the Transformer-CNN Bridge (TCB)– envisioned to *fuse* the aggregated quality embeddings of a transformer backbone with hierarchical feature representations of CNNs. We implement TCB as an adaptive re-calibration block that learns which feature channels to emphasize, and then use convolution operations to extract their local dependencies.

We validate the proposed concepts with comprehensive experiments; our **DGIQA** model achieves SOTA performance on NR-IQA benchmark datasets of both synthetic (LIVE [41], CSIQ [26], TID2013 [36], Kadid10k [29]) and authentic (LIVE-C [13], KonIQ10k [18] and LIVE-FB [62]) image distortions. Moreover, DGIQA outperforms the SOTA models by considerable margins on cross-dataset evaluations and unseen natural scenes. Our ablation experiments reveal that these improvements are attributed to the multimodal feature learning by TCB blocks and depth-guided feature distillation by Depth-CAR. We further conduct qualitative and quantitative analyses of the generalization performance of DGIQA on low-light imaging and enhancement datasets: LOL [10], D2G [25], Flare7k [11], IHAZE [2], and GoPro [35]. These datasets include unseen images with low-light effects, hazy conditions, and lens flares – which DGIQA can assess and separate over 41% better than SOTA models on all four datasets; see Fig. 2.

The main contributions of this paper are summarized below:

- 1) We present a novel NR-IQA model named **DGIQA** which incorporates scene depth to improve NR-IQA learning of structure-level distortions related to focus, blurriness, and other geometric artifacts. We propose

a *Depth-CAR* mechanism that enables this by learning a projection function to dynamically refine feature representations based on depth cues, which improves both robustness and efficiency.

- 2) We designed a *Transformer-CNN Bridge (TCB)* block that effectively bridges global information of patch embeddings of Transformers with local hierarchical features extracted by CNNs for improved IQA learning.
- 3) Comprehensive experiments on benchmark datasets, cross-dataset evaluation, and ablation studies demonstrate the effectiveness of our proposed model and learning pipeline. Specifically, DGIQA achieves SOTA performance on benchmark datasets and outperforms existing models in assessing unseen image distortions.

We also present a new evaluation criteria for IQA generalization performance, by ‘*density separation*’ of predicted scores on high-quality versus distorted images. As Fig. 2 shows, we demonstrate that unseen data from other imaging domains can be used to validate NR-IQA generalization.

## 2. NR-IQA Literature and Related Work

Classical NR-IQA methods rely on handcrafted features and statistical models for IQA without reference images, with subjective IQA databases as a reliable proxy for objective IQA scores. Early approaches use the Natural Scene Statistics (NSS) [12, 14, 33, 34, 60, 66] to exploit statistical regularities in natural images to detect deviations caused by distortions. BRISQUE (blind image spatial quality evaluator) [33] and BLIINDS (blind image integrity notator using DCT statistics) [38] are prominent metrics that demonstrate robust IQA performance in most scenarios. Besides, HOSA [55] and CORNIA [61] deploy a *code book* list of local features as a reference for guided IQA. These metrics are widely used for their simplicity and efficiency. However, they generally fail to capture complex natural distortions due to limited feature representations and sensitivity to domain shifts. With the advent of deep learning, data-driven approaches [4, 23, 32] have been dominating the benchmarks for both subjective and objective IQA learning.

**CNNs and GAN-based Models.** CNNs are powerful feature extractors that learn hierarchical spatial dependencies from large-scale data, which are crucial to infer image quality [3, 22, 30, 43, 44, 54, 70, 74]. Canonical approaches like CNNIQA [23] and WaDiQaM [4] demonstrated that CNNs outperform statistical approaches in extracting discriminative features for robust IQA. In recent years, HyperIQA [43] reported much-improved performance by learning multi-scale hierarchical features using a context-aware hypernetwork. DBCNN [70] employed a *seimese* architecture to capture authentic and synthetic distortions, subsequently improving the model’s adaptability to various distortions. MetaIQA [74] proposed a way to learn prior knowledge with two distortion types by meta-learning. Contemporary

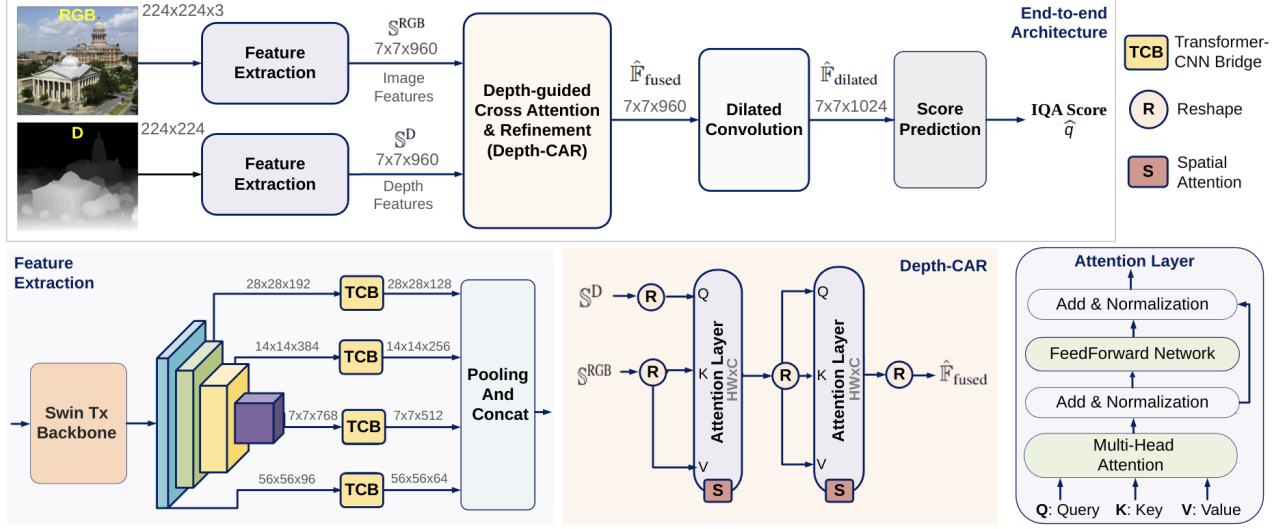


Figure 3. The model architecture of **DGIQA** is shown; major learning components are: two pre-trained Swin Transformer backbones for hierarchical feature extraction from input image (RGB) and depth (D); Transformer-CNN Bridge (TCB) blocks for dominant feature distillation; depth-guided cross-attention (**Depth-CAR**) for RGB-D feature fusion; and a dilated convolution stack – for NR-IQA learning.

methods further report better generalization with domain-aware NR-IQA [54] across different distortion levels.

**Transformer-based Approaches.** ViTs efficiently capture long-range dependencies across different parts of an image. IQT [63] demonstrated that transformers induce less locality bias than CNNs and offer better IQA predictions across large databases. MUSIQ [24] can retain the original image shape by looking up image patches in a 2-D hash map. TRaS [15] calculates the consistency loss and relative ranking between images and uses a transformer encoder to enhance the final predictions. MANIQA [59] achieves SOTA performance by integrating a ViT with a multi-dimensional attention mechanism, which helps capture global contextual information for accurately assessing perceptual image distortions. However, ViTs often lack the inductive biases necessary for capturing local texture details for detecting fine-grained distortions. Vision-language fusion frameworks [9, 47, 53, 71] are recently being explored to address this issue, although it remains an open problem.

### 3. Proposed method

#### 3.1. End-to-end IQA Learning

The proposed DGIQA model is designed to capture both global contextual features and local geometric cues for comprehensive IQA. The end-to-end learning pipeline is presented in Fig. 3; given an Image  $\mathbf{I}^{\text{RGB}} \in \mathbb{R}^{H \times W \times 3}$  and corresponding depth map  $\mathbf{I}^{\text{D}} \in \mathbb{R}^{H \times W}$ , the objective is to learn its IQA prediction score. We use two swin transformers in parallel to extract hierarchical features for each modality; let the extracted features be denoted as  $\mathbf{F}_i^{\text{RGB}}$  and  $\mathbf{F}_i^{\text{D}}$ , respectively where  $i=1, 2, 3, 4$  indicating the 4 stages of the backbone feature maps. These feature maps are propa-

gated through four Transformer-CNN Bridge (TCB) blocks to further extract the local dependencies for distilling the most important features for IQA learning; see Fig. 4.

The TCB-distilled features are spatially downsampled, aligned to match dimensions, and concatenated to form the combined feature maps  $\mathbf{S}^{\text{RGB}}$  and  $\mathbf{S}^{\text{D}}$ . We then use a multi-head cross-attention block for depth-guided learning of the object saliency and structural information about the input scene. Specifically, we use the  $\mathbf{S}^{\text{D}}$  features as *queries* to extract geometric cues from  $\mathbf{S}^{\text{RGB}}$  as *keys*; this mechanism is followed by self-attention for further refinement.

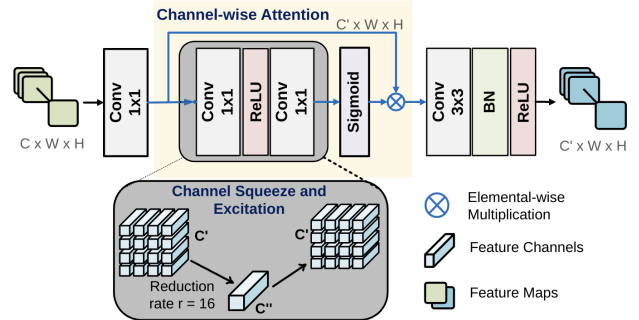


Figure 4. The proposed TCB architecture is shown; it performs a CNN-based projection (resolving local hierarchical dependencies) from the Swin Tx features (capturing global patch-level contexts).

The refined feature map ( $\hat{\mathbf{F}}^{\text{fused}}$ ) is then passed through a dilated convolution stack [64] that has two Conv layers with dilation rates of 2 and 4. This helps to expand the receptive field aims to extract multi-scale contextual features from  $\hat{\mathbf{F}}^{\text{fused}}$ . The last stage applies a global average pooling that compress the final feature maps and propagates it to a fully connected layer for predicting final IQA scores  $\hat{q}$ .

### 3.2. Transformer-CNN Bridge (TCB)

Transformer-based backbones employ attention mechanisms that can capture global dependencies and contextual relevance between distant image patches. Besides, CNNs capture spatial hierarchies and local patterns with progressive convolution layers. Our design intuition for TCB is to take advantage of the transformer features to learn which channels to emphasize, and then use convolution operations to get their local hierarchical dependencies. As shown in Fig. 4, we envision an adaptive recalibration of channel-wise features while retaining local spatial information through convolutions. To achieve this, we employ the *squeeze-and-excitation* mechanism [19], where at first, a  $1 \times 1$  Conv layer projects the backbone (Swin Tx) extracted features  $\mathbb{F}_i^{\text{RGB}}$  and  $\mathbb{F}_i^{\text{D}}$  from channel size  $C=(96,192,384,768)$  into  $C'=(64,128,256,512)$ , respectively; this helps reduce the computational overhead and required training time in the channel attention stage.

The second  $1 \times 1$  Conv refers to the *squeeze* operation, which projects  $C'$  to  $C''=(4,8,16,32)$  channels by a reduction rate  $r=16$ . This compresses the information across channels to create a more compact representation; ReLU activation is applied to introduce non-linearity. A third  $1 \times 1$  Conv is applied for *excitation*, which expands the channel dimension from  $C''$  back to  $C'$  by learning the respective attention weights. After that, it is passed through a Sigmoid ( $\sigma$ ) to ensure that the attention weights are in  $[0, 1]$ . These weights are element-wise multiplied with the original feature map to emphasize the most important channels. While *squeeze-and-excitation* focuses on channel-wise importance, a subsequent  $3 \times 3$  convolution extracts local spatial dependencies to capture finer details. The filtered features are then passed through batch normalization (BN) and ReLU, completing the TCB-based feature project process as:

$$\mathbb{A} = \sigma(\text{Conv}_{1 \times 1}(\text{ReLU}(\text{Conv}_{1 \times 1}(\mathbb{F}_{\text{in}})))), \quad (1)$$

$$\mathbb{F}_{\text{out}} = \text{ReLU}(\text{BN}(\text{Conv}_{3 \times 3}(\mathbb{F}_{\text{in}} \otimes \mathbb{A}))). \quad (2)$$

Here,  $\mathbb{A}$  is the projected attention map and  $\mathbb{F}_{\text{in}}$  ( $\mathbb{F}_{\text{out}}$ ) are the input (output) feature maps, respectively.

### 3.3. Depth-guided Cross-Attention & Refinement

The Depth-CAR block exploits depth features to learn object saliency and structural information from the RGB features for improved IQA predictions. We employ an attention mechanism with queries  $Q = \mathbb{S}^{\text{D}} \mathbf{W}_Q$  selected from the depth features, while the keys  $K = \mathbb{S}^{\text{RGB}} \mathbf{W}_K$  and values  $V = \mathbb{S}^{\text{RGB}} \mathbf{W}_V$  that come from the RGB features. Here,  $\mathbf{W}_K$ ,  $\mathbf{W}_Q$ , and  $\mathbf{W}_V$  are learned projection matrices that guide the attention over RGB features to emphasize structural details and object saliency in the input scene.

With this setup, the attention mechanism is computed us-

ing scaled dot-product attention given as follows:

$$\text{Attention}(Q, K, V) = \text{Softmax}\left(\frac{QK^{\top}}{\sqrt{d_k}}\right)V \quad (3)$$

where  $d_k$  is the embedding dimension. By depth-based queries, our model can focus on closer objects and salient regions in the image, emulating human visual perception that naturally prioritizes nearby prominent object features.

Our depth-guided CAR approach is inspired by recent advancements in the cross-modal attention mechanism for RGB-D feature fusion in semantic segmentation and image registration literature [42, 73]. We extend the core idea by using spatial attention to emphasize important  $\mathbb{S}^{\text{RGB}}$  features queried by  $\mathbb{S}^{\text{D}}$  features. We further refine the fused features by self-attention blocks as outlined in the original transformer architecture [46]. We use another spatial attention layer for this refinement to capture long-range dependencies within the cross-attended feature maps.

### 3.4. Dilation Convolution Block

The dilation convolution block in our model is designed to increase the receptive field of the network without losing resolution. It leverages dilated (atrous) convolutions [64], which introduce spaces between the Conv filter elements, effectively allowing it to cover a wider area without increasing parameters or reducing the spatial dimensions of the feature maps. We employ two consecutive dilated convolutions with dilation rates 2 and 4, each followed by batch normalization (BN) and ReLU operations, as follows:

$$\hat{\mathbb{F}}_{\text{dilated}} = \text{ReLU}(\text{BN}(\text{Conv}_{3 \times 3, \text{dtn}=2,4}(\hat{\mathbb{F}}_{\text{fused}}))). \quad (4)$$

### 3.5. Score Prediction

Finally, IQA prediction is performed by projecting the  $\hat{\mathbb{F}}_{\text{dilated}}$  feature maps into a scalar score  $\hat{q}$ . After global average pooling condenses the spatial dimensions, the pooled feature vector  $\mathbb{F}_{\text{pooled}}$  is passed through a fully connected (FC) layer to generate the predicted score  $\hat{q} \in [0, 1]$  through a sigmoid activation; specifically,

$$\hat{q} = \sigma(\mathbf{W}_{\text{fc}} \cdot \mathbb{F}_{\text{pooled}} + \mathbf{b}_{\text{fc}}) \quad (5)$$

where  $\mathbf{W}_{\text{fc}}$  and  $\mathbf{b}_{\text{fc}}$  are the learnable weights and biases of the FC layer, and  $\sigma$  is the sigmoid function.

### 3.6. Loss Functions

We use two loss functions for the supervised training of DGIQA. The primary loss is the Mean-Squared Error (MSE) between the predicted and ground truth scores as:  $\mathcal{L}_{\text{MSE}} = \frac{1}{N} \sum_{n=1}^N (q_n - \hat{q}_n)^2$ , where  $N$  is the sample batch size. Additionally, a **Consistency Loss** (CL) inspired by TRES [15] is introduced to ensure generalized learning consistency; it measures the MSE between the predicted score of the original image and its horizontally flipped version



$\hat{q}_n^{\text{FLIP}}$ . Specifically,  $\mathcal{L}_{\text{CL}} = \frac{1}{N} \sum_{n=1}^N (\hat{q}_n - \hat{q}_n^{\text{FLIP}})^2$ . With these two loss terms, our objective function is given by

$$\mathcal{L}_{\text{Total}} = \mathcal{L}_{\text{MSE}} + \lambda \mathcal{L}_{\text{CL}} \quad (6)$$

Here,  $\lambda$  is an empirically tuned hyper-parameter that balances the contribution of the consistency loss.

## 4. Benchmark Evaluation

### 4.1. Dataset and Evaluation Criteria

For comprehensive performance evaluation of DGIQA, we perform the experiments on seven benchmark datasets: LIVE[41], CSIQ[26], TID2013[36], Kadid10k[29], LIVE Challenge[13], Koniq10k[18], and LIVE-FB[62]. Each dataset consists of images with varying distortions, and their corresponding ground truth scores, which are derived from subjective estimates by human assessors and are categorized into Mean Opinion Scores (MOS) or Differential Mean Opinion Scores (DMOS). We regularize the scores between 0 (totally distorted) and 1 (original image). Table 1 shows a summary information on all the datasets.

Table 1. Information on benchmark datasets used in the training and evaluation of DGIQA.

Dataset	Types	# Images	# Distortions	Scores
LIVE	Synthetic	982	5	DMOS
CSIQ	Synthetic	866	6	DMOS
TID2013	Synthetic	3,000	24	MOS
Kadid10k	Synthetic	10,125	25	DMOS
Live Challenge	Authentic	1,162	-	MOS
Koniq10k	Authentic	10,073	-	MOS
LIVE-FB	Authentic	39,810	-	MOS

**Evaluation Metrics.** We use two standard metrics [52, 65]: Spearman’s rank order correlation coefficient (SROCC) and Pearson’s linear correlation coefficient (PLCC) to evaluate the correlation between the predicted scores and the true scores of the distorted pictures. PLCC is defined as:

$$PLCC = \frac{\sum_{i=1}^N (\hat{q}_i - \bar{\hat{q}})(q_i - \bar{q})}{\sqrt{\sum_{i=1}^N (\hat{q}_i - \bar{\hat{q}})^2} \sqrt{\sum_{i=1}^N (q_i - \bar{q})^2}}$$

where  $N$  is the number of distorted images,  $\hat{q}_i$  is the predicted scores,  $q_i$  is the true scores, and  $\bar{\hat{q}}$  and  $\bar{q}$  are the corresponding means. Besides, SROCC is defined as:

$$SROCC = 1 - \frac{6 \sum_{i=1}^N d_i^2}{N(N^2 - 1)}$$

where  $d_i$  is the pairwise differences between  $q_i$  and  $\hat{q}_i$ .

### 4.2. Implementation details

We implement DGIQA using PyTorch libraries, with a NVIDIA A100 GPU for training and evaluation. Following standard practices [59, 74], we address varying input sizes

by taking random  $224 \times 224$  crops from the image and depth map instead of resizing during training. The DepthAnything model [58] is used for generating depth pairs when ground truth is not available. Data augmentation includes horizontal and vertical flips applied uniformly (with a probability of 0.5). We use the albumentation library [5] to ensure RGB-D alignment during data augmentation.

The two Swin Transformer (Swin-T) backbones [31] of DGIQA are pre-trained on ImageNet-21k dataset to (learn to) extract multi-scale feature maps from RGB and depth inputs. We use AdamW optimizer with a weight decay of  $1e^{-2}$  and a learning rate of  $1e^{-4}$  ( $1e^{-5}$ ) for synthetic (authentic) datasets. The learning rate schedule follows a Cosine Annealing strategy [57] where  $T_{max}$  is set to half the number of total epochs at which point the learning rate reaches its minimum value of  $1e^{-7}$ . The maximum training duration is set to 200 epochs. The batch size is set to 16 to balance the memory cost and training stability. Following the usual IQA training practice, the dataset is split 80:20, repeated 10 times with different seeds; the mean SROCC and PLCC scores are then reported for evaluation.

### 4.3. Performance Comparison With SOTA

**Dataset Evaluation.** The benchmark datasets (Table 1) include a diverse range of images with various types and levels of distortions, enabling a comprehensive objective evaluation of how closely a model’s predictions align with human perception. Table 2 presents the performance of our DGIQA model in terms of SROCC and PLCC, compared to SOTA models across synthetic and authentic datasets. Our model consistently ranks within the **top two** and notably achieves the **best performance** on LIVE, CSIQ, Kadid10k, LIVE-C, and Koniq10k datasets. Such consistent scores across these diverse datasets validate the robustness and effectiveness of DGIQA learning pipeline.

**Cross-dataset Evaluation.** In many real-world applications, image quality distortions can vary significantly from those seen during training. Cross-dataset evaluation helps examine how well an NR-IQA model performs on entirely different datasets with unique images, distortion types, and quality levels. This evaluation approach helps reveal overfitting tendencies as well. We evaluate the performance of DGIQA through comprehensive cross-dataset evaluations on both synthetic and authentic datasets. Results are reported in Table 3 showing that our model **outperforms the SOTA models** in most dataset pairs. Specifically, DGIQA achieves 0.79%-2.80% (3.86%-6.41%) improvements on SROCC (PLCC) scores on authentic datasets. The corresponding improvements on synthetic datasets are 2.64%-4.96% (0.41%-4.78%) for SROCC (PLCC) scores, respectively. As Table 3 indicates, our DGIQA exhibits a strong generalization across diverse scenes and distortion types, verifying its robustness and learning effectiveness.

Table 2. SROCC and PLCC results comparison of DGIQA against SOTA NR-IQA models on synthetic and authentic datasets are shown. Top two scores are marked in **blue**; the best scores are **bold**; ‘-’ indicates the model checkpoints and results are not available/reported.

Model	Synthetic Datasets								Authentic Datasets					
	LIVE		CSIQ		TID2013		Kadid10k		Live-Challenge		Koniq10k		LIVE-FB	
	SROCC	PLCC	SROCC	PLCC	SROCC	PLCC	SROCC	PLCC	SROCC	PLCC	SROCC	PLCC	SROCC	PLCC
DIIVINE [38]	0.892	0.908	0.804	0.776	0.643	0.567	0.413	0.435	0.588	0.591	0.546	0.558	0.092	0.187
BRISQUE [33]	0.929	0.944	0.812	0.748	0.626	0.571	0.528	0.567	0.629	0.629	0.681	0.685	0.303	0.341
HyperIQA [43]	0.962	0.966	0.923	0.942	0.840	0.858	0.852	0.845	0.872	0.885	0.906	0.917	0.544	0.602
MUSIQ [24]	0.940	0.911	-	-	0.773	0.815	0.875	0.872	0.702	0.746	0.916	0.928	0.566	0.661
TReS [15]	0.969	0.968	0.922	0.942	0.863	0.883	0.859	0.858	0.846	0.877	0.915	0.928	0.554	0.625
MANIQA [59]	<b>0.982</b>	<b>0.983</b>	<b>0.968</b>	0.961	<b>0.937</b>	<b>0.943</b>	<b>0.944</b>	<b>0.943</b>	0.871	0.887	0.880	0.915	0.543	0.597
Re-IQA [39]	0.970	0.971	0.947	0.960	0.804	0.861	0.872	0.885	0.840	0.854	0.914	0.923	<b>0.645</b>	<b>0.733</b>
LoDa [56]	0.975	0.979	0.958	0.965	0.869	0.901	0.931	0.936	0.876	0.899	<b>0.932</b>	<b>0.944</b>	0.578	0.679
ARNIQA [1]	0.966	0.972	0.962	<b>0.973</b>	0.880	0.901	0.908	0.912	-	-	-	-	<b>0.595</b>	0.671
LIQE [72]	0.970	0.951	0.936	0.939	-	-	0.931	0.930	<b>0.904</b>	<b>0.910</b>	0.919	0.908	-	-
CLIPQA <sup>+</sup> [47]	0.948	0.952	0.907	0.928	0.835	0.857	0.913	0.909	0.805	0.832	0.895	0.909	0.540	0.566
TOPIQ [6]	-	-	-	-	-	-	-	-	0.870	0.884	0.926	0.939	<b>0.652</b>	<b>0.745</b>
<b>DGIQA (ours)</b>	<b>0.982</b>	<b>0.981</b>	<b>0.971</b>	<b>0.976</b>	<b>0.934</b>	<b>0.940</b>	<b>0.943</b>	<b>0.945</b>	<b>0.891</b>	<b>0.910</b>	<b>0.934</b>	<b>0.942</b>	0.591	0.685

Table 3. Cross-dataset performance of DGIQA is shown in comparison with the closest competitors: MANIQA, LoDa, and other models that report good cross-validation IQA results; ‘-’ indicates the model checkpoints and results are not available/reported.

(a) Evaluation on authentic datasets.						
Train On	Koniq10K				LIVE-FB	
Test On	LIVE-C		LIVE-FB		Koniq10K	
Model ↓	SROCC	PLCC	SROCC	PLCC	SROCC	PLCC
TReS [15]	0.786	<b>0.803</b>	<b>0.453</b>	<b>0.559</b>	0.703	0.713
MANIQA [59]	0.792	0.807	0.405	0.438	-	-
ARNIQA [1]	0.723	0.758	0.410	0.486	0.738	<b>0.749</b>
LoDa [56]	<b>0.811</b>	-	-	-	<b>0.763</b>	-
<b>DGIQA</b>	<b>0.808</b>	<b>0.834</b>	<b>0.462</b>	<b>0.515</b>	<b>0.769</b>	<b>0.797</b>
(b) Evaluation on synthetic datasets.						
Train On	Kadid10k				TID2013	
Test On	LIVE		TID2013		LIVE	
Model ↓	SROCC	PLCC	SROCC	PLCC	SROCC	PLCC
HyperIQA [43]	<b>0.908</b>	-	0.706	-	0.876	-
TReS [15]	0.894	0.872	0.701	0.726	0.857	0.842
MANIQA [59]	0.865	0.820	0.700	<b>0.730</b>	-	-
ARNIQA [1]	0.898	<b>0.900</b>	<b>0.760</b>	0.715	<b>0.887</b>	<b>0.880</b>
<b>DGIQA</b>	<b>0.932</b>	<b>0.909</b>	<b>0.724</b>	<b>0.733</b>	<b>0.931</b>	<b>0.922</b>

#### 4.4. Ablation Experiments

We perform several ablation studies to demonstrate the effectiveness of major computational components of DGIQA. We analyze our model performance with and without TCB blocks, Depth-CAR, and dilated convolution blocks – in comparison with the full model. Fig. 5 illustrates the effectiveness of our multimodal learning, Table 4 presents the results for the LIVE-C, and Table 5 presents the cross-dataset validation on LIVE-C and LIVE-FB datasets with models trained on the Koniq10K dataset alone.

Table 4. Ablation results on LIVE-C dataset are shown for four configurations of the proposed DGIQA model.

Cfg	TCB	Depth-CAR	Dilation	SROCC	PLCC	# Params
#1	✓		✓	0.877	0.902	65 M
#2	✓	✓		0.888	0.907	103 M
#3		✓	✓	0.890	0.907	127 M
#4	✓	✓	✓	<b>0.891</b>	<b>0.909</b>	<b>103 M</b>



Figure 5. A few instances of Grad-CAM [40] visualizations of DGIQA model’s attention (from the dilated stack) are shown, demonstrating more guided attention on salient objects when depth is used for training, compared to using RGB inputs alone.

**Effects of Depth Fusion.** To demonstrate the effectiveness of incorporating depth information in our learning pipeline, we use Grad-Cam [40] to generate heatmaps that visualize regions where DGIQA focuses for IQA predictions. We show a few comparisons in Fig. 5, which clearly illustrates that depth information guides our model to focus on salient objects [20], leading to more accurate predictions that align closely with how human visual perception works. In contrast, without depth information, the model’s attention is more dispersed and less targeted.

Table 4 further demonstrates that Depth-Guided CAR improves DGIQA performance by 1.6% (0.8%) in SROCC (PLCC). It also boosts the cross-dataset performance by 3.2% (2.2%) on LIVE-C, and 8.2% (5.3%) on LIVE-FB in SROCC (PLCC), respectively; see Table 5.

**Impacts of TCB Blocks.** As mentioned earlier, TCB blocks are envisioned to exploit the Swin Tx features to capture more local interactions with the subsequent Conv opera-

Table 5. Cross-dataset ablation results of DGIQA trained on Koniq10K alone (for the same 4 configurations of Table 4).

Test On → Model Configurations ↓	LIVE-C		LIVE-FB	
	SROCC	PLCC	SROCC	PLCC
#1. DGIQA (w/o D-CAR)	0.783	0.816	0.427	0.489
#2. DGIQA (w/o Dilation)	0.804	0.830	0.431	0.490
#3. DGIQA (w/o TCB)	0.806	0.828	0.457	0.509
#4. <b>DGIQA (Full)</b>	<b>0.808</b>	<b>0.834</b>	<b>0.462</b>	<b>0.515</b>

tions. Then, it prioritizes the relevant channels for IQA predictions by its squeeze-and-excitation mechanism. We observe that these process downsamples feature maps, thus reducing the learnable parameters without compromising performance. As Table 4 and Table 5 demonstrate, the addition of TCB blocks increases overall NR-IQA performance, while **reducing the model parameters by 23.3%**. Effectively, it saves one-fifth of the training and inference time in addition to boosting net NR-IQA performance.

**Contributions of Dilated Convolution.** Dilated convolutions introduce gaps between pixels in the convolutional filters, effectively widening the receptive field. This enables the model to capture information from a broader context. As Table 5 demonstrates, dilation stacks increase overall performance by 0.5% (0.5%) on LIVE-C and 7.2% (5.1%) on LIVE-FB dataset in SROCC (PLCC) scores, respectively.

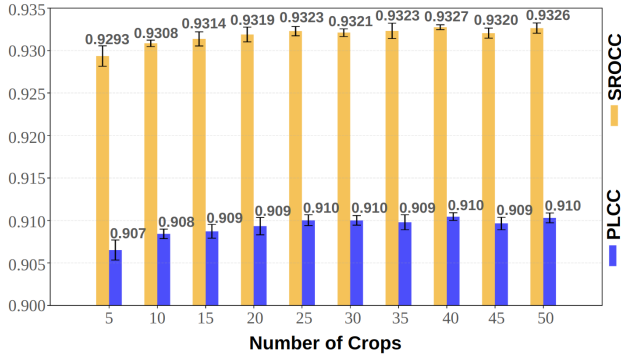


Figure 6. Cross-dataset ablation results based on different numbers of crops, trained on Kadid10k and tested on LIVE dataset.

**Impacts of Hyper-parameters.** Fig. 6 presents the cross-validation performance with a varied number of crops selected for evaluation. We select 25 crops as a balance between performance and validation time. We also investigate the impacts of the contribution factor of the consistency loss,  $\lambda$  (see Eq. 6); 0.3 gives the best results while corner values towards 0 and 1 reduce the performance. More detailed results are in Appendix A.

## 5. Generalized IQA Learning

### 5.1. Effective Feature Distillation

We now investigate the feature distillation capabilities as well as the separability and overlap of DGIQA-predicted

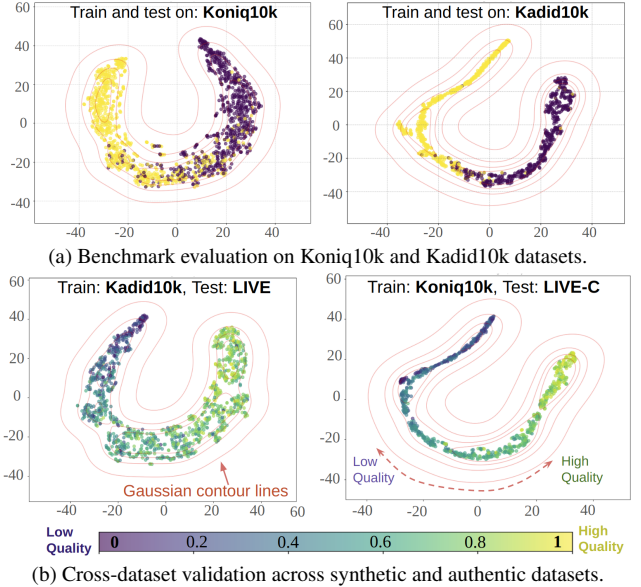


Figure 7. Feature projections of the final DGIQA layer with t-SNE visualizations (color bar indicates normalized MOS scores).

IQA scores. We use t-distributed stochastic neighbor embedding (t-SNE [45]) to visualize the high-dimensional feature representations of DGIQA in a 2D space. In Fig. 7a, we visually inspect the clustering patterns related to different image quality levels for two large datasets: Koniq10k and Kadid10k. As seen, both visualizations reveal characteristic *horseshoe patterns*, with distinct separation and smooth progression in quality levels highlighting that DGIQA effectively learns robust and transferable quality-aware features. The same pattern is visible for cross-validation results on LIVE and LIVE-C, as shown in Fig. 7b. The **horseshoe contours are more acute** in the cross-dataset visualization, indicating that DGIQA can learn discriminative features that capture nuanced differences between image quality in unseen distortion types.

### 5.2. Performance on Natural Image Distortions

To further demonstrate our model’s generalization capabilities, we evaluated it on five datasets containing a diverse collection of natural distortions such as low light effects, lens flare, haze, and motion blur. We make use of benchmark datasets in other imaging domains, specifically: (i) LOL [10] and D2G [25] datasets consisting of well-lit and low-light images with varying quality; (ii) Flare7k [11] dataset containing images with artificially added lens flare; (iii) IHAZE [2] dataset with high-quality (clear) images paired with corresponding low-quality (hazy) images; and (iv) GoPro [35] dataset having high-quality images paired with low-quality images distorted by motion blur.

For these experiments, we train DGIQA and a few prominent SOTA models on the Koniq10k dataset. For eval-



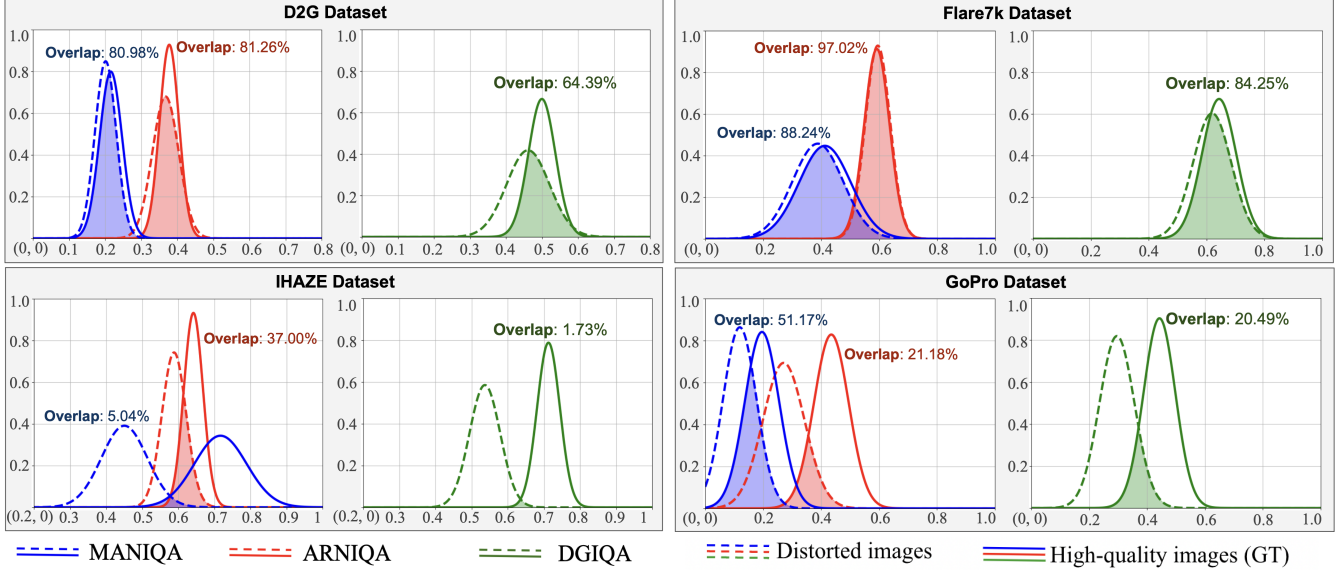


Figure 8. Density separation of predicted IQA scores by DGIQA, SOTA transformer model (MANIQA), and CNN-based model (ARNIQA) are shown for four natural image distortion datasets: D2G, Flare7k, IHAZE, and GOPRO; results for LOL data is in Fig. 2. Significantly lower overlap between high-quality and distorted images demonstrates a superior generalization performance of DGIQA.

uation, we compute scores for both high-quality (ground truth) and low-quality (distorted) images and represent them as separate Gaussian distributions. Our intuition is that a well-generalized model would produce distinct distributions with less overlap between the two distributions. To this end, we propose this ‘density separation’ as a **new evaluation criterion** for NR-IQA generalization performance. Fig. 8 illustrates the results for DGIQA and two SOTA models: MANIQA [59] and ARNIQA [1] as baselines.

**Analyses and Discussion.** As shown in Fig. 8, DGIQA achieves significantly better density separation across all datasets. Compared to the SOTA baselines, our model demonstrates 41-50%, 20-21%, 5-13%, 65-95%, and 3-60% less overlaps in LOL, D2G, Flare7k, IHAZE, and GOPRO datasets, respectively. Note that the subtle differences caused by lens flare make Flare7k the most challenging dataset, where all models experience significant overlap. Nevertheless, DGIQA still outperforms the baseline performance by considerable margins. It showcases the strongest generalization performance on the IHAZE dataset, achieving only 1.73% overlap. We hypothesize that although hazy effects degrade RGB information, depth features remain relatively stable, enabling DGIQA to perceive structural cues for more discriminative IQA learning. The consistent generalization performance of our model is more apparent from the qualitative results in Fig. 9 and Appendix C.

**Limitations and Challenges.** While DGIQA demonstrates strong performances across various IQA tasks, it faces limitations in scenarios where scene depth is too noisy or not

informative. For images with no significant depth variation (e.g., on uniformly textured surfaces, flat landscapes) or images captured from a single focal plane, the depth guidance does not improve IQA performance. In some cases, Depth-CAR fails to project useful features, causing model divergence. Another challenge is that strong backbone feature extractors increase the computational demands, limiting off-the-shelf use in real-time applications. Nevertheless, model compression (quantization, low-rank factorization) operations can generate *light versions* to balance the robustness-efficiency trade-off for real-time use.

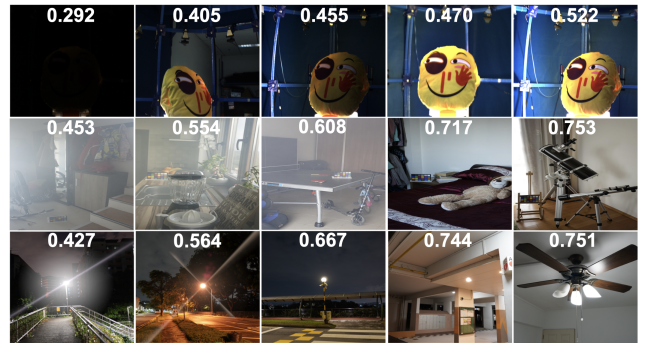


Figure 9. Consistent IQA predictions of DGIQA are shown for: (top row) low-light effects, (middle) haze, and (bottom row) lens flares – with decreasing levels of distortions from left to right.

**Additional Results.** Supplementary results, ablation studies, and analyses are in the Appendix section. Moreover, DGIQA model and inference code are available at: <https://github.com/uf-robopi/DGIQA>



## 6. Conclusion

In this paper, we introduce DGIQA, a novel approach to NR-IQA that integrates Transformers' patch-level embeddings with CNN hierarchical features through Transformer-CNN Bridges (TCBs) for comprehensive feature distillation. We also incorporate multimodal IQA learning with depth-guided cross-attention and refinement (Depth-CAR) to focus on salient objects and structural details, enhancing IQA performance. The projection functions in TCBs reduce model parameters by 23.3%, while still achieving SOTA performance. DGIQA demonstrates strong generalization, surpassing SOTA models in cross-dataset validations and assessing unseen natural distortions. Future works will explore a computationally light version of DGIQA for real-time video content moderation and filtering applications.

## Acknowledgment

This work is supported in part by the National Science Foundation (NSF) award #2330416 and the University of Florida (UF) research grant #132763.

## References

- [1] Lorenzo Agnolucci, Leonardo Galteri, Marco Bertini, and Alberto Del Bimbo. Arnika: Learning Distortion Manifold for Image Quality Assessment. In *Proceedings of the IEEE/CVF Winter Conference on Applications of Computer Vision*, pages 189–198, 2024. 2, 6, 8, 15
- [2] Codruta O. Ancuti, Cosmin Ancuti, Radu Timofte, and Christophe De Vleeschouwer. I-HAZE: A Dehazing Benchmark With Real Hazy and Haze-Free Indoor Images. In *arXiv:1804.05091v1*, 2018. 2, 7, 15
- [3] Simone Bianco, Luigi Celona, Paolo Napoletano, and Ramondo Schettini. On the Use of Deep Learning for Blind Image Quality Assessment. *Signal, Image and Video Processing*, 12:355–362, 2018. 2
- [4] Sebastian Bosse, Dominique Maniry, Klaus-Robert Müller, Thomas Wiegand, and Wojciech Samek. Deep Neural Networks for No-Reference and Full-Reference Image Quality Assessment. *IEEE Transactions on image processing*, 27(1):206–219, 2017. 2
- [5] Alexander Buslaev, Vladimir I. Iglovikov, Eugene Khvedchenya, Alex Parinov, Mikhail Druzhinin, and Alexandr A. Kalinin. Albumentations: Fast and Flexible Image Augmentations. *Information*, 11(2), 2020. 5
- [6] Chaofeng Chen, Jiadi Mo, Jingwen Hou, Haoning Wu, Liang Liao, Wenxiu Sun, Qiong Yan, and Weisi Lin. TOPIQ: A Top-down Approach from Semantics to Distortions for Image Quality Assessment, 2023. 6
- [7] Hao Chen and Youfu Li. Progressively Complementarity-Aware Fusion Network for RGB-D Salient Object Detection. In *2018 IEEE/CVF Conference on Computer Vision and Pattern Recognition*, pages 3051–3060, 2018. 1
- [8] Hao Chen, Youfu Li, and Dan Su. Multi-modal fusion network with multi-scale multi-path and cross-modal interactions for RGB-D salient object detection. *Pattern Recognition*, 86:376–385, 2019. 1
- [9] Zewen Chen, Haina Qin, Juan Wang, Chunfeng Yuan, Bing Li, Weiming Hu, and Liang Wang. PromptIQA: Boosting the Performance and Generalization for No-Reference Image Quality Assessment via Prompts. In *European Conference on Computer Vision*, pages 247–264. Springer, 2025. 3
- [10] Chen Wei, Wenjing Wang, Wenhan Yang, Jiaying Liu. Deep Retinex Decomposition for Low-Light Enhancement. In *British Machine Vision Conference*, 2018. 2, 7
- [11] Yuekun Dai, Chongyi Li, Shangchen Zhou, Ruicheng Feng, and Chen Change Loy. Flare7K: A Phenomenological Night-time Flare Removal Dataset. In *Thirty-sixth Conference on Neural Information Processing Systems Datasets and Benchmarks Track*, 2022. 2, 7, 15
- [12] Xinbo Gao, Fei Gao, Dacheng Tao, and Xuelong Li. Universal Blind Image Quality Assessment Metrics Via Natural Scene Statistics and Multiple Kernel Learning. *IEEE Transactions on neural networks and learning systems*, 24(12), 2013. 2
- [13] Deepti Ghadiyaram and Alan C Bovik. Massive Online Crowdsourced Study of Subjective and Objective Picture Quality. *IEEE Transactions on Image Processing*, 25(1):372–387, 2015. 2, 5, 12, 14
- [14] Deepti Ghadiyaram and Alan C Bovik. Perceptual Quality Prediction on Authentically Distorted Images Using a Bag of Features Approach. *Journal of vision*, 17(1):32–32, 2017. 2
- [15] S Alireza Golestaneh, Saba Dadsetan, and Kris M Kitani. No-Reference Image Quality Assessment Via Transformers, Relative Ranking, and Self-Consistency. In *Proceedings of the IEEE/CVF winter conference on applications of computer vision*, pages 1220–1230, 2022. 3, 4, 6
- [16] Paul B Hibbard, Alice E Haines, and Rebecca L Hornsey. "Magnitude, Precision, and Realism of Depth Perception in Stereoscopic Vision". *Cogn. Res. Princ. Implic.*, 2(1):25, May 2017. 1
- [17] Alain Horé and Djemel Ziou. Image Quality Metrics: PSNR vs. SSIM. In *2010 20th International Conference on Pattern Recognition*, pages 2366–2369, 2010. 15
- [18] Vlad Hosu, Hanhe Lin, Tamas Sziranyi, and Dietmar Saupe. KonIQ-10k: An Ecologically Valid Database for Deep Learning of Blind Image Quality Assessment. *IEEE Transactions on Image Processing*, 29:4041–4056, 2020. 2, 5
- [19] Jie Hu, Li Shen, and Gang Sun. Squeeze-and-Excitation Networks. In *Proceedings of the IEEE conference on computer vision and pattern recognition*, pages 7132–7141, 2018. 4
- [20] Md Jahidul Islam, Ruobing Wang, and Junaed Sattar. SVAM: Saliency-guided Visual Attention Modeling by Autonomous Underwater Robots. In *Robotics: Science and Systems (RSS)*, NY, USA, 2022. 6, 12
- [21] Ding Jia, Jianyuan Guo, Kai Han, Han Wu, Chao Zhang, Chang Xu, and Xinghao Chen. GeminiFusion: Efficient Pixel-wise Multimodal Fusion for Vision Transformer, 2024. 2
- [22] Tao Jiang, Xiao-juan Hu, Xing-hua Yao, Li-ping Tu, Jing-bin Huang, Xu-xiang Ma, Ji Cui, Qing-feng Wu, and Jia-tuo Xu. Tongue Image Quality Assessment Based on a Deep Convolutional Neural Network. *BMC Medical Informatics and Decision Making*, 21(1):147, 2021. 2
- [23] Le Kang, Peng Ye, Yi Li, and David Doermann. Convo-

- lutional Neural Networks for No-Reference Image Quality Assessment. In *Proceedings of the IEEE conference on computer vision and pattern recognition*, pages 1733–1740, 2014. 2
- [24] Junjie Ke, Qifei Wang, Yilin Wang, Peyman Milanfar, and Feng Yang. Musiq: Multi-Scale Image Quality Transformer. In *Proceedings of the IEEE/CVF international conference on computer vision*, pages 5148–5157, 2021. 3, 6
- [25] Rizwan Khan, You Yang, Qiong Liu, and Zahid Hussain Qaisar. Divide and Conquer: Ill-Light Image Enhancement Via Hybrid Deep Network. *Expert Systems with Applications*, 182:115034, 2021. 2, 7, 15
- [26] Eric C Larson and Damon M Chandler. Most Apparent Distortion: Full-Reference Image Quality Assessment and The Role of Strategy. *Journal of electronic imaging*, 19(1):011006–011006, 2010. 2, 5, 14, 15
- [27] Shuang Li, Zewei Yang, and Hongsheng Li. Statistical Evaluation of No-Reference Image Quality Assessment Metrics For Remote Sensing Images. *ISPRS International Journal of Geo-Information*, 6(5):133, 2017. 1
- [28] Jingyun Liang, Jiezhong Cao, Guolei Sun, Kai Zhang, Luc Van Gool, and Radu Timofte. Swinir: Image Restoration Using Swin Transformer. In *Proceedings of the IEEE/CVF international conference on computer vision*, pages 1833–1844, 2021. 1
- [29] Hanhe Lin, Vlad Hosu, and Dietmar Saupe. KADID-10k: A Large-Scale Artificially Distorted IQA Database. In *Eleventh International Conference on Quality of Multimedia Experience (QoMEX)*, pages 1–3. IEEE, 2019. 2, 5, 14, 15
- [30] Kwan-Yee Lin and Guanxiang Wang. Hallucinated-IQA: No-Reference Image Quality Assessment Via Adversarial Learning. In *Proceedings of the IEEE conference on computer vision and pattern recognition*, pages 732–741, 2018. 2
- [31] Ze Liu, Yutong Lin, Yue Cao, Han Hu, Yixuan Wei, Zheng Zhang, Stephen Lin, and Baining Guo. Swin Transformer: Hierarchical Vision Transformer Using Shifted Windows. In *Proceedings of the IEEE/CVF International Conference on Computer Vision*, pages 10012–10022, 2021. 5
- [32] Kede Ma, Wentao Liu, Kai Zhang, Zhengfang Duanmu, Zhou Wang, and Wangmeng Zuo. End-to-End Blind Image Quality Assessment Using Deep Neural Networks. *IEEE Transactions on Image Processing*, 27(3):1202–1213, 2017. 2
- [33] Anish Mittal, Anush Krishna Moorthy, and Alan Conrad Bovik. No-Reference Image Quality Assessment in the Spatial Domain. *IEEE Transactions on image processing*, 21(12):4695–4708, 2012. 2, 6
- [34] Anush Krishna Moorthy and Alan Conrad Bovik. Blind Image Quality Assessment: From Natural Scene Statistics to Perceptual Quality. *IEEE transactions on Image Processing*, 20(12):3350–3364, 2011. 2
- [35] Seungjun Nah, Tae Hyun Kim, and Kyoung Mu Lee. Deep Multi-Scale Convolutional Neural Network for Dynamic Scene Deblurring. In *Proceedings of the IEEE conference on computer vision and pattern recognition*, pages 3883–3891, 2017. 2, 7, 15
- [36] Nikolay Ponomarenko, Lina Jin, Oleg Ieremeiev, Vladimir Lukin, Karen Egiazarian, Jaakko Astola, Benoit Vozel, Kacem Chehdi, Marco Carli, Federica Battisti, et al. Image Database TID2013: Peculiarities, Results and Perspectives. *Signal processing: Image communication*, 30:57–77, 2015. 2, 5, 14, 15
- [37] Ekta Prashnani, Hong Cai, Yasamin Mostofi, and Pradeep Sen. PieAPP: Perceptual Image-Error Assessment Through Pairwise Preference. In *2018 IEEE/CVF Conference on Computer Vision and Pattern Recognition*, pages 1808–1817, 2018. 15
- [38] Michele A Saad, Alan C Bovik, and Christophe Charrier. Blind Image Quality Assessment: A Natural Scene Statistics Approach in the DCT Domain. *IEEE transactions on Image Processing*, 21(8):3339–3352, 2012. 1, 2, 6
- [39] Avinab Saha, Sandeep Mishra, and Alan C Bovik. Re-iqu: Unsupervised Learning for Image Quality Assessment In the Wild. In *Proceedings of the IEEE/CVF conference on computer vision and pattern recognition*, pages 5846–5855, 2023. 6, 15
- [40] Ramprasaath R. Selvaraju, Michael Cogswell, Abhishek Das, Ramakrishna Vedantam, Devi Parikh, and Dhruv Batra. Grad-CAM: Visual Explanations from Deep Networks via Gradient-Based Localization. In *2017 IEEE International Conference on Computer Vision (ICCV)*, pages 618–626, 2017. 6, 15, 17
- [41] Hamid R Sheikh, Muhammad F Sabir, and Alan C Bovik. A Statistical Evaluation of Recent Full Reference Image Quality Assessment Algorithms. *IEEE Transactions on image processing*, 15(11):3440–3451, 2006. 2, 5, 12, 15
- [42] Xinrui Song, Hanqing Chao, Xuan Xu, Hengtao Guo, Sheng Xu, Baris Turkbey, Bradford J. Wood, Thomas Sanford, Ge Wang, and Pingkun Yan. Cross-Modal Attention for Multi-Modal Image Registration. *Medical Image Analysis*, 82:102612, 2022. 4
- [43] Shaolin Su, Qingsen Yan, Yu Zhu, Cheng Zhang, Xin Ge, Jinqui Sun, and Yanning Zhang. Blindly Assess Image Quality in the Wild Guided by a Self-Adaptive Hyper Network. In *Proceedings of the IEEE/CVF conference on computer vision and pattern recognition*, pages 3667–3676, 2020. 2, 6
- [44] Hossein Talebi and Peyman Milanfar. NIMA: Neural Image Assessment. *IEEE transactions on image processing*, 27(8):3998–4011, 2018. 2
- [45] Laurens Van der Maaten and Geoffrey Hinton. Visualizing Data Using t-SNE. *Journal of machine learning research*, 9(11), 2008. 7
- [46] Ashish Vaswani, Noam Shazeer, Niki Parmar, Jakob Uszkoreit, Llion Jones, Aidan N. Gomez, Łukasz Kaiser, and Illia Polosukhin. Attention is All You Need. In *Advances in Neural Information Processing Systems*, volume 30, pages 5998–6008. Curran Associates, Inc., 2017. 4
- [47] Jianyi Wang, Kelvin CK Chan, and Chen Change Loy. Exploring Clip for Assessing the Look and Feel of Images. In *Proceedings of the AAAI Conference on Artificial Intelligence*, volume 37, pages 2555–2563, 2023. 3, 6
- [48] Lanjiang Wang. A Survey on IQA. *arXiv preprint arXiv:2109.00347*, 2021. 1
- [49] Xintao Wang, Liangbin Xie, Chao Dong, and Ying Shan. Real-esrgan: Training Real-world Blind Super-resolution With Pure Synthetic Data. In *Proceedings of the IEEE/CVF international conference on computer vision*, pages 1905–

- 1914, 2021. 1
- [50] Zhou Wang and Alan Conrad Bovik. *Modern Image Quality Assessment*. PhD thesis, Springer, 2006. 1
- [51] Zhou Wang, Alan C Bovik, and Ligang Lu. Why Is Image Quality Assessment So Difficult? In *IEEE International conference on acoustics, speech, and signal processing*, volume 4, pages IV–3313. IEEE, 2002. 1
- [52] Zhou Wang, Alan C Bovik, Hamid R Sheikh, and Eero P Simoncelli. Image Quality Assessment: From Error Visibility to Structural Similarity. *IEEE transactions on image processing*, 13(4):600–612, 2004. 5, 12, 15
- [53] Tianhe Wu, Kede Ma, Jie Liang, Yujiu Yang, and Lei Zhang. A Comprehensive Study of Multimodal Large Language Models for Image Quality Assessment. *arXiv preprint arXiv:2403.10854*, 2024. 3
- [54] Weihao Xia, Yujiu Yang, Jing-Hao Xue, and Jing Xiao. Domain Fingerprints for No-Reference Image Quality Assessment. *IEEE Transactions on Circuits and Systems for Video Technology*, 31(4):1332–1341, 2020. 2, 3
- [55] Jingtao Xu, Peng Ye, Qiaohong Li, Haiqing Du, Yong Liu, and David Doermann. Blind Image Quality Assessment Based on High Order Statistics Aggregation. *IEEE Transactions on Image Processing*, 25(9):4444–4457, 2016. 2
- [56] Kangmin Xu, Liang Liao, Jing Xiao, Chaofeng Chen, Haoning Wu, Qiong Yan, and Weisi Lin. Boosting Image Quality Assessment through Efficient Transformer Adaptation with Local Feature Enhancement. In *Proceedings of the IEEE/CVF Conference on Computer Vision and Pattern Recognition*, pages 2662–2672, 2024. 6
- [57] Junfeng Yang, Jing Fu, Zhen Zhang, Limei Liu, Qin Li, Wei Zhang, and Wenzhi Cao. Align-IQA: Aligning Image Quality Assessment Models with Diverse Human Preferences via Customizable Guidance. In *Proceedings of the 32nd ACM International Conference on Multimedia*, pages 10008–10017, 2024. 5, 15
- [58] Lihe Yang, Bingyi Kang, Zilong Huang, Xiaogang Xu, Jiashi Feng, and Hengshuang Zhao. Depth Anything: Unleashing the Power of Large-Scale Unlabeled Data. In *Proceedings of the IEEE/CVF Conference on Computer Vision and Pattern Recognition*, pages 10371–10381, 2024. 5, 12, 17
- [59] Sidi Yang, Tianhe Wu, Shuwei Shi, Shanshan Lao, Yuan Gong, Mingdeng Cao, Jiahao Wang, and Yujiu Yang. Maniqa: Multi-Dimension Attention Network for No-Reference Image Quality Assessment. In *Proceedings of the IEEE/CVF Conference on Computer Vision and Pattern Recognition*, pages 1191–1200, 2022. 2, 3, 5, 6, 8
- [60] Peng Ye and David Doermann. No-Reference Image Quality Assessment Using Visual Codebooks. *IEEE Transactions on Image Processing*, 21(7):3129–3138, 2012. 2
- [61] Peng Ye, Jayant Kumar, Le Kang, and David Doermann. Unsupervised Feature Learning Framework for No-Reference Image Quality Assessment. In *IEEE conference on computer vision and pattern recognition*, pages 1098–1105. IEEE, 2012. 2
- [62] Zhenqiang Ying, Haoran Niu, Praful Gupta, Dhruv Mahajan, Deepti Ghadiyaram, and Alan Bovik. From Patches to Pictures (PaQ-2-PiQ): Mapping the Perceptual Space of Picture Quality. In *Proceedings of the IEEE/CVF conference on computer vision and pattern recognition*, pages 3575–3585, 2020. 2, 5, 12, 14
- [63] Junyong You and Jari Korhonen. Transformer for Image Quality Assessment. In *IEEE international conference on image processing (ICIP)*, pages 1389–1393. IEEE, 2021. 3
- [64] F Yu. Multi-Scale Context Aggregation By Dilated Convolutions. *arXiv preprint arXiv:1511.07122*, 2015. 3, 4
- [65] Guangtao Zhai and Xiongkuo Min. Perceptual Image Quality Assessment: A Survey. *Science China Information Sciences*, 63:1–52, 2020. 1, 5, 12
- [66] Lin Zhang, Lei Zhang, and Alan C Bovik. A Feature-Enriched Completely Blind Image Quality Evaluator. *IEEE Transactions on Image Processing*, 24(8):2579–2591, 2015. 2
- [67] Lin Zhang, Lei Zhang, Xuanqin Mou, and David Zhang. FSIM: A Feature Similarity Index for Image Quality Assessment. *IEEE transactions on Image Processing*, 20(8):2378–2386, 2011. 15
- [68] Qiang Zhang, Qi Qin, Yang Yang, Qiang Jiao, and Jungong Han. Feature Calibrating and Fusing Network for RGB-D Salient Object Detection. *IEEE Transactions on Circuits and Systems for Video Technology*, 34(3):1493–1507, 2024. 1
- [69] Richard Zhang, Phillip Isola, Alexei A Efros, Eli Shechtman, and Oliver Wang. The Unreasonable Effectiveness of Deep Features as a Perceptual Metric. In *CVPR*, 2018. 15
- [70] Weixia Zhang, Kede Ma, Jia Yan, Dexiang Deng, and Zhou Wang. Blind Image Quality Assessment Using a Deep Bilinear Convolutional Neural Network. *IEEE Transactions on Circuits and Systems for Video Technology*, 30(1):36–47, 2018. 2
- [71] Weixia Zhang, Guangtao Zhai, Ying Wei, Xiaokang Yang, and Kede Ma. Blind Image Quality Assessment Via Vision-Language Correspondence: A Multitask Learning Perspective. In *Proceedings of the IEEE/CVF conference on computer vision and pattern recognition*, pages 14071–14081, 2023. 3
- [72] Weixia Zhang, Guangtao Zhai, Ying Wei, Xiaokang Yang, and Kede Ma. Blind Image Quality Assessment via Vision-Language Correspondence: A Multitask Learning Perspective. In *IEEE Conference on Computer Vision and Pattern Recognition*, pages 14071–14081, 2023. 6
- [73] Wujie Zhou, Yuxiang Xiao, Weiqing Yan, and Lu Yu. CMPFFNet: Cross-Modal and Progressive Feature Fusion Network for RGB-D Indoor Scene Semantic Segmentation. *IEEE Transactions on Automation Science and Engineering*, 21(4):5523–5533, 2024. 2, 4
- [74] Hancheng Zhu, Leida Li, Jinjian Wu, Weisheng Dong, and Guangming Shi. MetaQA: Deep Meta-Learning for No-Reference Image Quality Assessment. In *Proceedings of the IEEE/CVF conference on computer vision and pattern recognition*, pages 14143–14152, 2020. 2, 5

## Appendix

### A. Hyperparameter Tuning

#### A.1. Number of Crops

Following up on our discussion in Sec. 4.4 (Ablation Experiments) of the paper, we further analyze the impact of the number of crops on evaluation time and performance. Figure 6 illustrates the effect of varying the number of crops on Spearman’s rank order correlation coefficient (SROCC) [52], Pearson’s linear correlation coefficient (PLCC) [65], and validation time, with model trained on Kadid10k and tested on LIVE dataset. Our results indicate that fewer crops significantly reduce validation time but yield lower SROCC/PLCC scores. As the number of crops increases, performance stabilizes around 25 crops with minimal fluctuations in scores, while validation time continues to rise. Thus, selecting 25 crops achieves consistently high performance on both metrics while maintaining a reasonable validation time, striking a practical balance between computational efficiency and prediction accuracy.

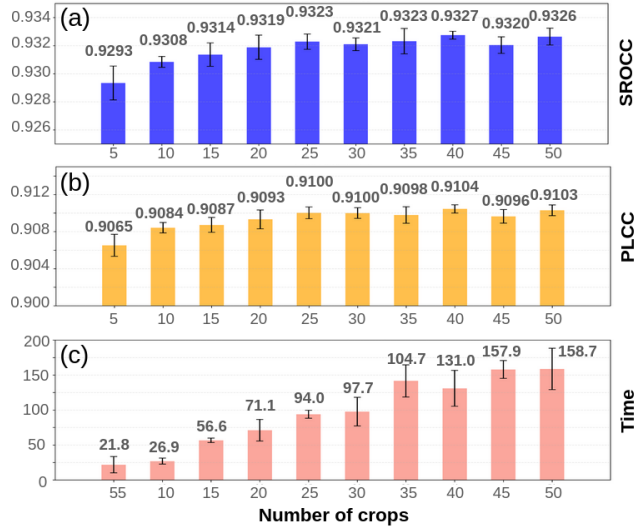


Figure 10. Cross-dataset ablation based on different numbers of crops, trained on Kadid10k and tested on LIVE dataset, are shown for (a) SROCC; (b) PLCC; (c) Validation time in milliseconds.

#### A.2. Contribution of the Consistency Loss

The objective function employed in our model, detailed in Section 3.6 (Loss Functions) of the paper, is defined as:

$$\mathcal{L}_{\text{Total}} = \mathcal{L}_{\text{SME}} + \lambda \mathcal{L}_{\text{CL}} \quad (7)$$

where  $\lambda$  is a hyperparameter that balances the contribution of the consistency loss,  $\mathcal{L}_{\text{CL}}$ .

Figure 11 illustrates the impact of varying  $\lambda$  on performance metrics for training and validation on the LIVE-C [13] dataset for one training seed, focusing on SROCC

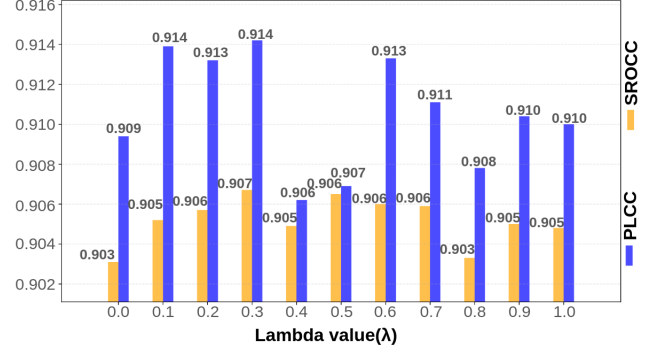


Figure 11. DGIQA performance on LIVE-C dataset for different consistency weights (of  $\lambda$ ).

and PLCC. The results indicate that the SROCC score reaches its minimum at  $\lambda = 0$ , while PLCC reaches its minimum at  $\lambda = 0.4$ . Both metrics achieve their maximum values when  $\lambda = 0.3$ . Due to image clarity constraints, we report results rounded to three decimal places; however, detailed trends can be observed from the bar chart. Overall, the results in Figure 11 demonstrate that setting  $\lambda = 0.3$  allows the model to achieve optimal performance by maximizing both correlation metrics.

### B. Distortion and Depth Images

Our proposed DGIQA model leverages distorted RGB images and their corresponding depth maps to enhance feature representation, facilitating improved IQA learning. To make the training process more effective and streamlined, we pre-compute all depth maps using DepthAnything [58] when ground truth depth maps are unavailable. Figure 12 illustrates examples from the LIVE [41] dataset, showcasing images subjected to five synthetic distortions: Fast Fading, Gaussian Blur, JPEG 2000, JPEG, and White Noise. Each row highlights how the corresponding depth maps effectively capture structural and geometric cues despite the varying levels of distortion (Levels 1-5). Depth maps for severe distortions (e.g., White Noise Level 5) clearly demonstrate degraded structural information, reflecting the impact of heavy noise on feature extraction.

Figure 13 provides examples from the LIVEFB [62] dataset, which contains two inherent categories of distortions: Motion Blur and Vocemotic\_AVA. The depth maps generated by DepthAnything reveal their ability to emphasize foreground regions, or *salient* objects, critical for human visual attention [20]. For instance, the Motion Blur examples (top rows) retain the structural outlines of dynamic objects, such as bicycles and people in motion, even when RGB images exhibit heavy blurring. Similarly, the Vocemotic\_AVA examples (bottom rows) showcase depth maps that capture distinct foreground elements, such as architectural structures, animals, or human figures, while providing a clear separation from the background.



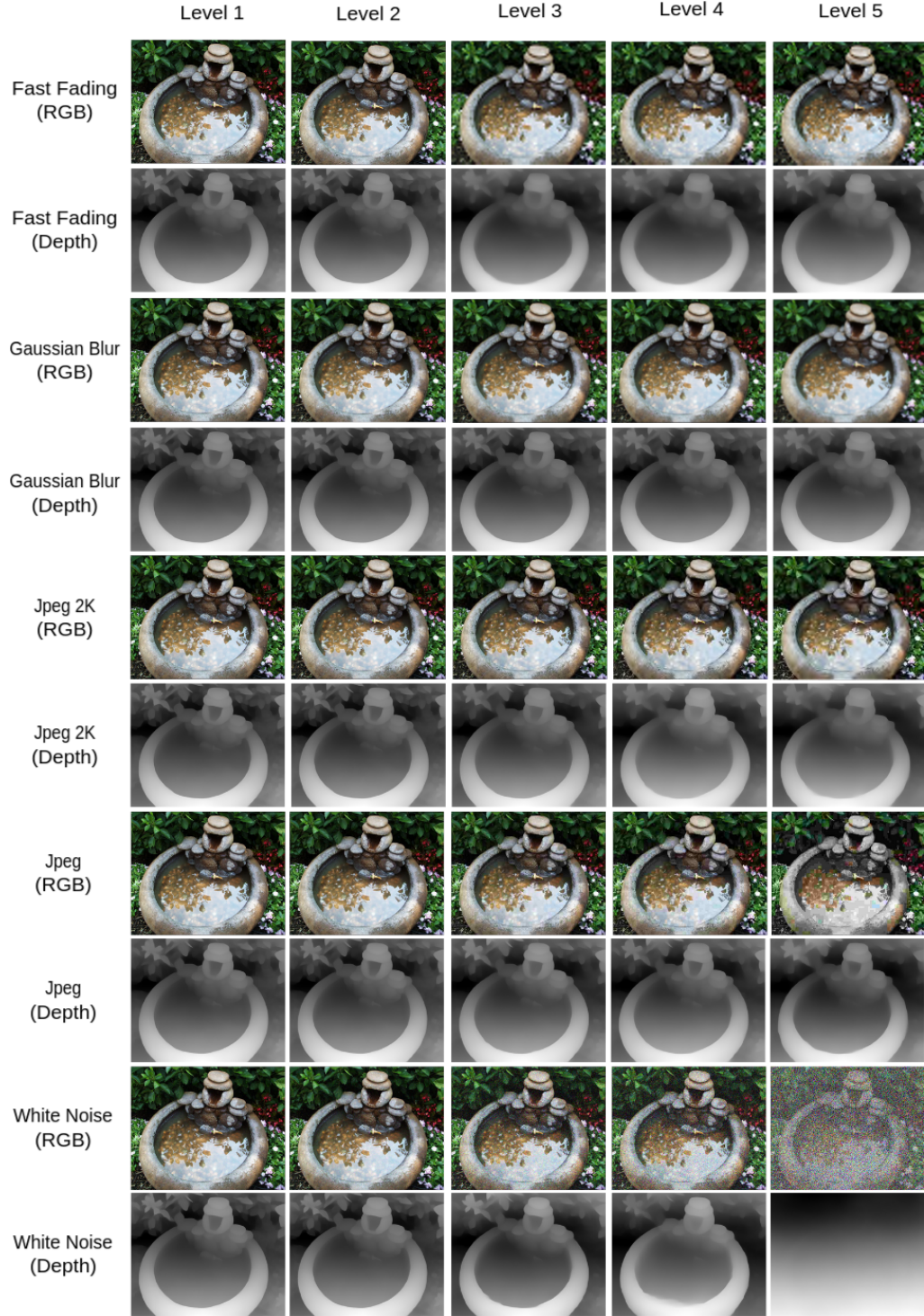


Figure 12. LIVE distortion images and their depth map samples. LIVE dataset includes 5 distortion types: Fast Fading, Gaussian Blur, JPEG 2K, JPEG, and White Noise, each having a distortion level from 1 (minimum distortion) to 5 (maximum distortion).

Notably, these depth maps consistently highlight salient regions across both synthetic and authentic distortions, demonstrating their robustness and utility in guiding the model to focus on visually significant areas. This capability

is essential for IQA, where human perception often prioritizes structural and semantic information in assessing image quality. The visualizations emphasize the effectiveness of integrating depth cues into the DGIQA learning pipeline,

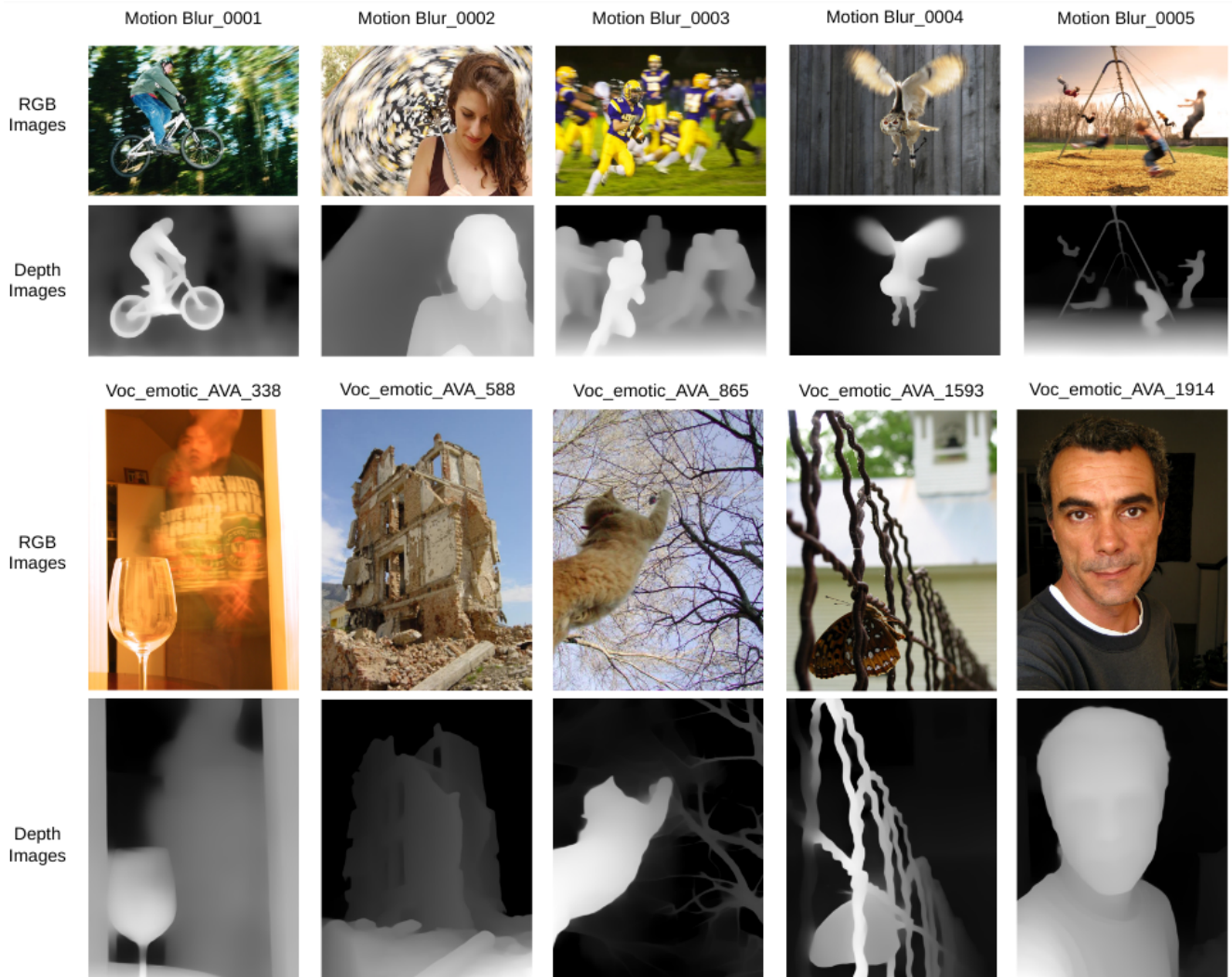


Figure 13. A few samples from the LIVE-FB synthetic distortion images and their depth maps are shown. Images are chosen from two inherent categories: Motion Blur and Voc\_emotic\_AVA.

enabling it to handle challenging distortion scenarios with improved accuracy and robustness.

## C. Additional Experiment Results

### C.1. Effective feature distillation

We present high-dimensional feature representations using t-distributed stochastic neighbor embeddings (t-SNE). Figure 14 visualizes feature embeddings from single-dataset training and testing on LIVE-C [13], CSIQ [26], TID2013 [36], and LIVE-FB [62], as well as cross-dataset evaluations where the model is trained on Kadid10k [29] and tested on TID2013, and trained on TID2013 and tested on LIVE. Each plot demonstrates the model’s ability to separate high-quality (yellow) and low-quality (purple) images, with the gradients representing intermediate-quality levels.

In single-dataset scenarios, t-SNE embeddings for

LIVE-C, CSIQ, TID2013, and LIVE-FB reveal distinct clustering of quality levels. LIVE-C shows clear distinctions between low- and high-quality images, with some overlap in intermediate scores. CSIQ and TID2013 exhibit “horseshoe” patterns indicating a smooth progression from low to high-quality embeddings. In cross-dataset evaluations, the embeddings demonstrate the model’s generalization capabilities. When trained on Kadid10k and tested on TID2013, feature separation remains robust, with high- and low-quality embeddings forming distinct clusters. Similarly, when trained on TID2013 and tested on LIVE, the embeddings maintain clear separation, though slightly more compact due to domain shift. These visualizations demonstrate DGIQA’s strong feature discrimination and generalization, consistently producing meaningful separations across synthetic, authentic, and cross-dataset scenarios.



Table 6. SROCC and PLCC results comparison of DGIQA against other IQA models on four benchmark datasets. The top two scores are highlighted in **blue**, with the best scores in **bold**.

Model	LIVE [41]		CSIQ [26]		TID2013 [36]		Kadid10k [29]	
	SROCC	PLCC	SROCC	PLCC	SROCC	PLCC	SROCC	PLCC
PSNR [17]	0.881	0.868	0.820	0.824	0.643	0.675	0.677	0.680
SSIM [52]	0.921	0.911	0.854	0.835	0.642	0.698	0.641	0.633
FSIM [67]	0.964	0.954	0.934	0.919	0.852	0.875	0.854	0.850
PieAPP [37]	0.915	0.905	0.900	0.881	0.877	0.850	0.869	0.869
LPIPS [69]	0.932	0.936	0.884	0.906	0.673	0.756	0.721	0.713
Re-IQA-FR [39]	0.969	0.974	0.961	0.962	0.920	0.921	0.933	0.936
ARNIQA-FR [1]	0.969	0.972	0.971	0.975	0.898	0.901	0.920	0.919
<b>DGIQA-FR (ours)</b>	<b>0.983</b>	<b>0.977</b>	<b>0.973</b>	0.963	<b>0.934</b>	<b>0.933</b>	<b>0.943</b>	<b>0.946</b>

## C.2. Grad-Cam visualizations

We integrated depth information into our model to enhance its focus on closer or salient objects, aligning more closely with human visual perception. Here, we present additional Grad-CAM [40] visualizations from the dilation convolution layer, comparing two model configurations: the full model with depth input and an ablated version without depth input (and without Depth-CAR module). Figure 15 presents additional examples that demonstrate how incorporating depth helps the model to focus on salient objects. These examples are categorized into two types of scenes: (i) scenes where the objects are positioned closer to the camera (Figure 15a), allowing the model to easily emphasize prominent features, and (ii) scenes containing distant objects (Figure 15b) with more depth variations.

The visualizations in Figure 15 validate that the full DGIQA model consistently allocates attention to foreground regions and salient objects, while the ablated model’s focus is more scattered. This consistent pattern across various scene types and distortion levels emphasizes the importance of depth information in guiding the model’s attention toward human-like perceptual evaluation.

## C.3. Full reference Image Quality Assessment

To further evaluate the effectiveness of our feature extractor, we conducted experiments to adapt our model for a Full Reference Image Quality Assessment (FR-IQA) task. The model architecture remains the same as in the NR-IQA setup. In this configuration, both the distorted image and its reference image are passed through the model to obtain their respective feature maps from the dilation convolution layer. The quality score,  $\hat{q}$  is then computed by taking the difference between these feature maps [39] and passing it through a fully connected (FC) layer, as follows:

$$\hat{q} = \sigma(\mathbf{W}_{\text{fc}} \cdot (\mathbb{F}_{\text{ref}} - \mathbb{F}_{\text{dist}}) + \mathbf{b}_{\text{fc}}) \quad (8)$$

where  $\mathbb{F}_{\text{ref}}$  and  $\mathbb{F}_{\text{dist}}$  are the feature maps of the reference and distorted images, respectively;  $\mathbf{W}_{\text{fc}}$  and  $\mathbf{b}_{\text{fc}}$  are the learn-

able weights and biases of the FC layer; and  $\sigma$  is the sigmoid function.

The training strategy for this experiment is kept similar to that of our NR-IQA learning, with the dataset split into an 80 : 20 ratio for training and testing. The experiment is repeated 10 times, and the mean SROCC and PLCC scores are computed as the final result. All other data augmentation and pre-processing steps are kept identical. We found that DGIQA-FR demonstrates faster convergence compared to DGIQA, requiring only 100 epochs. An initial learning rate of  $5e^{-5}$  is used, and a Cosine Annealing learning rate scheduler [57] is applied for smoother convergence.

Table 6 (see Page-4) presents the SROCC and PLCC results of our **DGIQA-FR** model, evaluated across four benchmark IQA datasets: LIVE, CSIQ, TID2013, and Kadid10k. For performance evaluation, we compare it against three closed-form metrics: PSNR [17], SSIM [52], and FSIM [67]; and four learning-based metrics: PieAPP [37], LPIPS [69], REIQA-FR [39], and ARNIQA-FR [1]. Among these, Re-IQA-FR and ARNIQA-FR were originally designed as NR-IQA models but were adapted for FR-IQA tasks in their respective works, serving as meaningful baselines for comparison. Without additional re-configuration or hyper-parameter tuning, our DGIQA-FR model demonstrates competitive results in both SROCC and PLCC across all four datasets. By performing comparably or better than other models, DGIQA-FR showcases its ability to adapt and generalize to FR-IQA tasks as well.

## C.4. External dataset predictions

Figure 16 showcases additional examples from natural image distortion datasets, highlighting the robustness of our DGIQA model across diverse real-world scenarios. The datasets include D2G [25] for low-light conditions, IHAZE [2] for hazy degradation, GoPro [35] for motion blur, and Flare7k [11] for light flares. Each row demonstrates the predicted scores of our model, effectively capturing the perceptual impact of varying distortions.

The first row illustrates samples from the D2G dataset, where images with progressively increasing light intensity

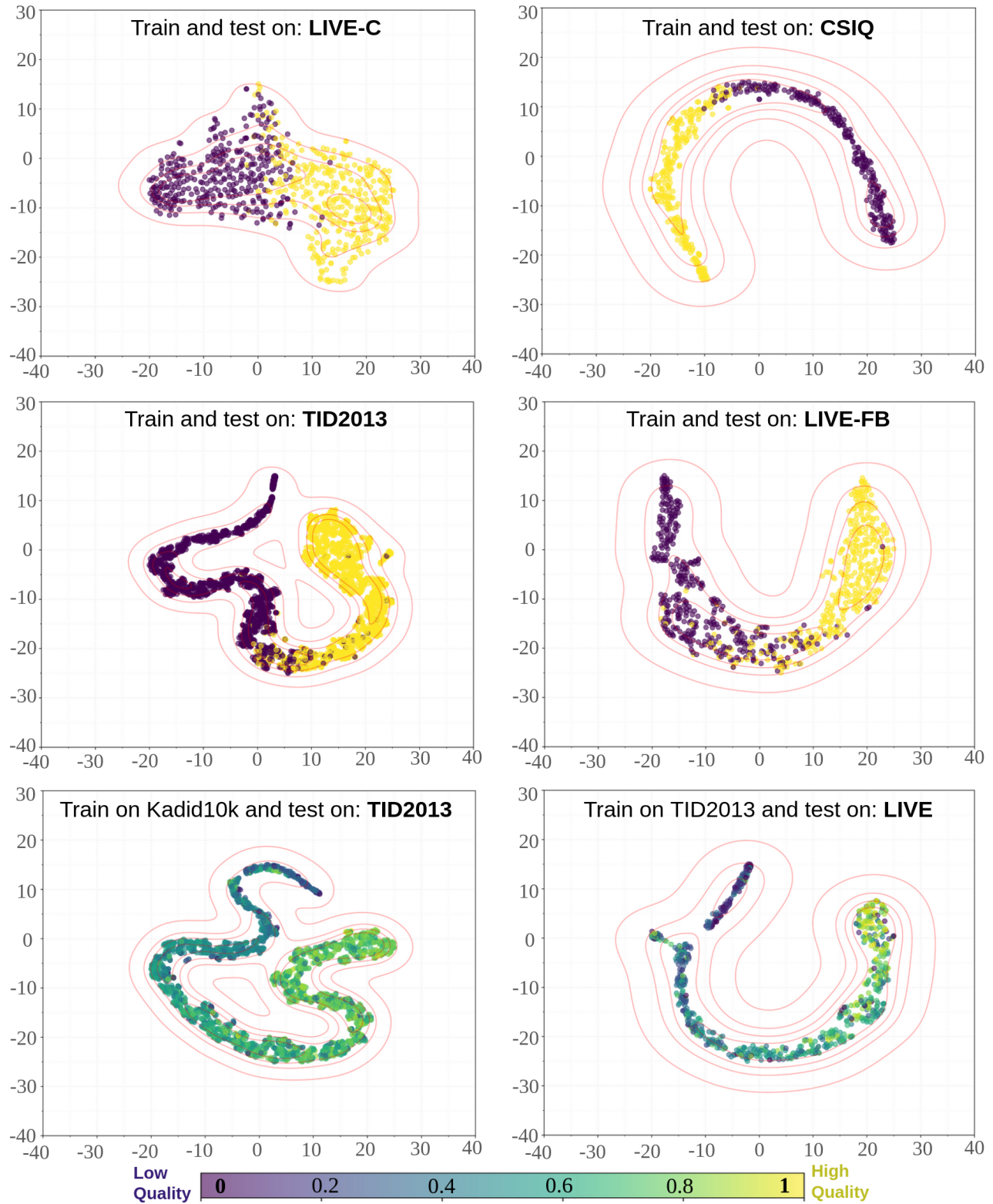
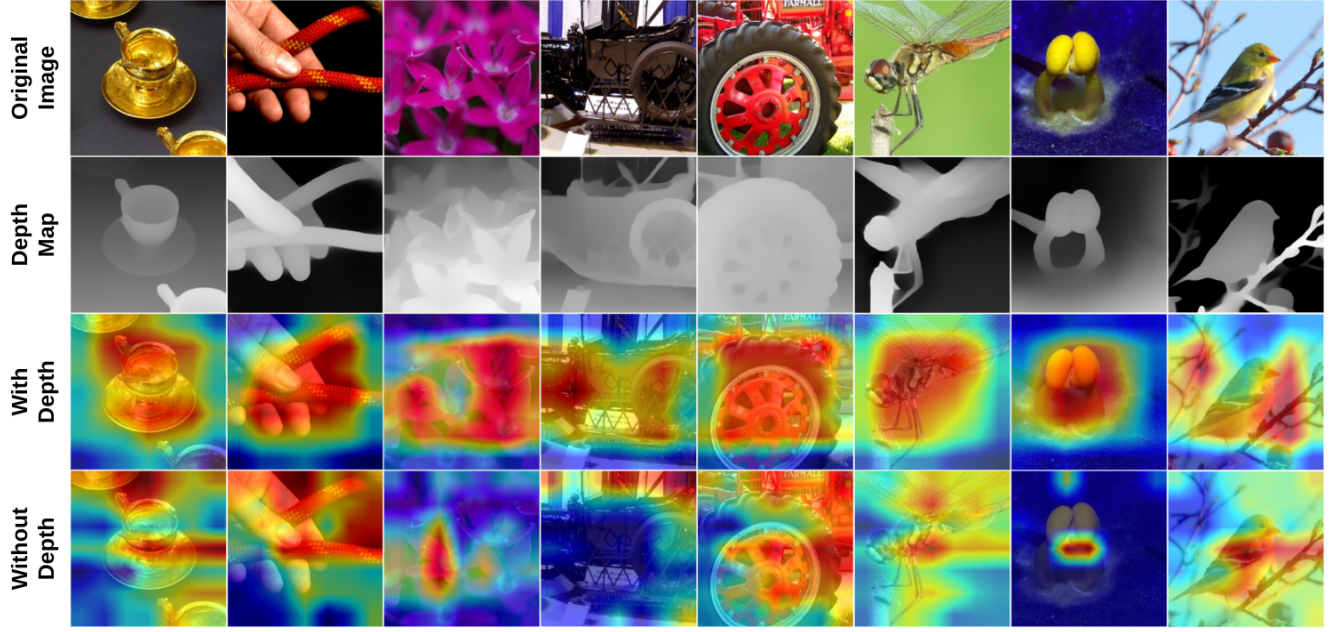
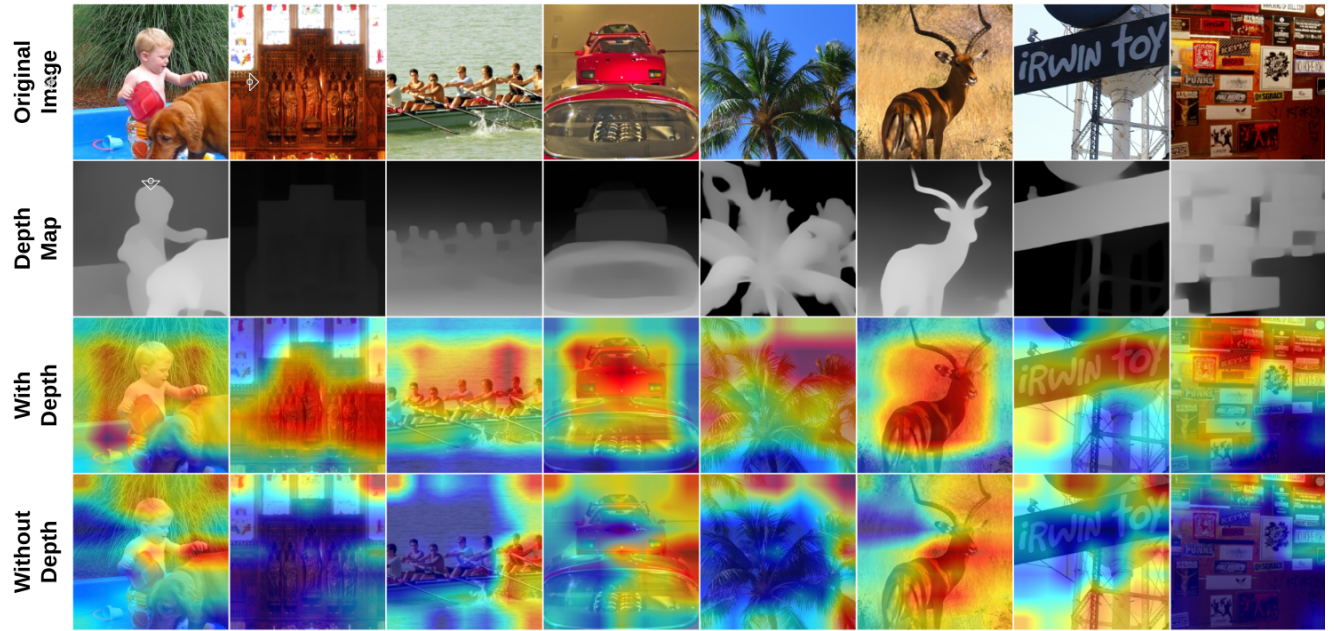


Figure 14. t-SNE visualizations of feature projections from the final DGIQA layer. For single-dataset tests, the visualization shows separations between "high-quality" and "low-quality" images. For cross-dataset tests, the visualization uses continuous colors to represent quality scores, ranging from 0 (completely distorted) to 1 (original image).





(a) Close-up scenes with a focus on dominant foreground objects.



(b) Scenes with distant objects and broader depth variations.

Figure 15. Additional examples of Grad-CAM [40] visualizations for the DGIQA model, highlighting the impact of depth. Each row displays the original RGB image, the Depth Map generated by DepthAnything [58], and the Grad-CAM outputs with and without depth input, respectively. (a) illustrates close-up scenes, while (b) features distant scenes with greater depth variations.

are shown. Our model’s predictions reflect an upward trend in quality scores as lighting improves, showcasing its sensitivity to perceptual clarity in low-light scenarios. However, excessive light can lead to distortions, as seen in the Flare7k examples (last two rows), where strong light flares reduce perceived quality. These examples validate DGIQA’s ability to identify degradation caused by unseen light scattering

patterns and brightness distortions caused by lens flares.

Besides, the third row presents hazy images from the IHAZE dataset, a natural distortion type. Despite varying haze densities, our model demonstrates consistent quality predictions, indicating its ability to process and evaluate structural and textural details obscured by haze. This robustness showcases DGIQA’s generalization performance

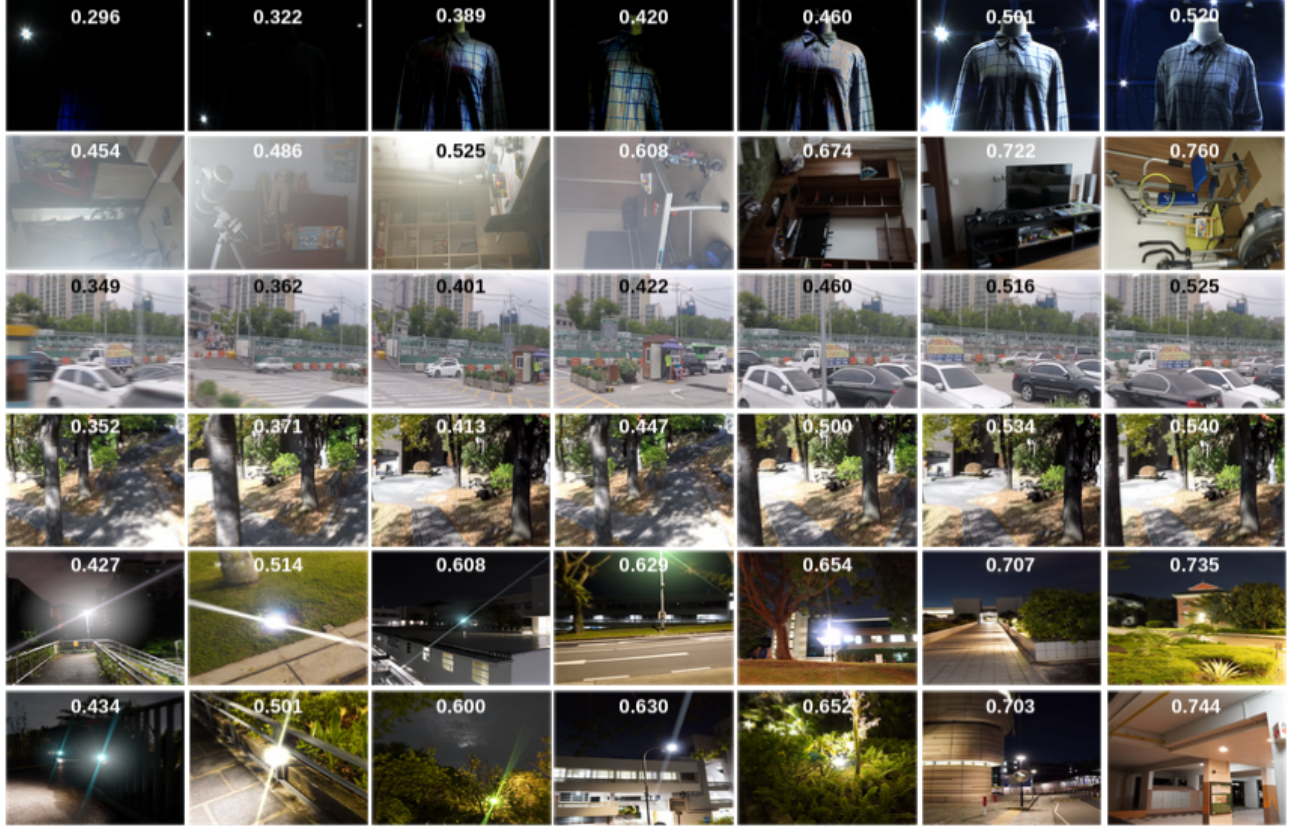


Figure 16. IQA predictions by our DGIQA model on unseen datasets: first row shows images from D2G dataset; second row from IHAZE dataset; third and fourth rows from GoPro dataset; fifth and sixth rows from Flare7k dataset. At each column, images are arranged with decreasing levels of distortion from left to right.

and adaptability to diverse natural scene conditions.

Finally, the fourth and fifth rows feature motion blur distortions from the GoPro dataset. Here, DGIQA effectively distinguishes between varying degrees of blur, assigning lower scores to heavily blurred images while improving scores for less degraded samples. These results demonstrate our model’s capacity to evaluate dynamic distortions and maintain robust predictions even in challenging scenarios involving motion. Although the Koniq10k dataset used for training includes a handful of images with motion blur, the number of such samples are limited (less than 50). Still, DGIQA is able to generalize well to the unseen levels of motion blurs of the GoPro dataset.

Overall, Figure 16 highlights the adaptability of our model to diverse and complex natural distortions. By consistently providing perceptually aligned quality scores across varied datasets, DGIQA demonstrates its capability to generalize effectively and tackle real-world scenarios, further solidifying its robustness and versatility in NR-IQA tasks.